General Decomposition Pathway of Organic–Inorganic Hybrid Perovskites through an Intermediate Superstructure and its Suppression Mechanism

Shulin Chen, Ying Zhang, Xiaowei Zhang, Jinjin Zhao,* Zewen Zhao, Xiao Su, Ze Hua, Jingmin Zhang, Jian Cao, Jicai Feng, Xiao Wang, Xinzheng Li, Junlei Qi,* Jiangyu Li,* and Peng Gao*

Organic–inorganic hybrid perovskites (OIHPs) have generated considerable excitement due to their promising photovoltaic performance. However, the commercialization of perovskite solar cells (PSCs) is still plagued by the structural degradation of the OIHPs. Here, the decomposition mechanism of OIHPs under electron beam irradiation is investigated via transmission electron microscopy, and a general decomposition pathway for both tetragonal $CH_3NH_3PbI_3$ and cubic $CH_3NH_3PbBr_3$ is uncovered through an intermediate superstructure state of $CH_3NH_3PbX_{2.5}$, X = I, Br, with ordered vacancies into final lead halides. Such decomposition can be suppressed via carbon coating by stabilization of the perovskite structure framework. These findings reveal the general degradation pathway of OIHPs and suggest an effective strategy to suppress it, and the atomistic insight learnt may be useful for improving the stability of PSCs.

Recent 10 years have witnessed a spectacular rise in power conversion efficiency of organic–inorganic hybrid perovskites (OIHPs) from initial 3.8%[1] to most recent 25.2%,[2] which shows its great potential as the efficient photovoltaic devices.[3] Yet the poor long-term stability issues of solar cells, which is mainly due to the degradation of the OIHPs, still hinder the further commercialization of the technology.[4,5] It has been reported that the OIHPs are easily decomposed under heating, electrical bias, and light illumination as well as exposure to oxygen and moisture.[6] For example, a temperature-dependent study shows that $CH_3NH_3PbI_3$ ($MAPbI_3$) decomposes to PbI_2 with the release of CH_3NH_2 and HI at 25–150 °C.[7] Synchrotron radiation analysis confirms the $MAPbI_3$ perovskite film decomposes to CH_3I, NH_3 and PbI_2 at 100 °C.[8] For the $MAPbI_3$-based solar cell, I⁻ and MA⁺ can diffuse into spiro-OMeTAD layer forming MAI and PbI_2 at 85 °C.[9] Under electrical bias, Jeangros et al. revealed that the iodide migrates into the positively biased charge transport layer and volatilizes along with the organic parts, leading to the formation of PbI_2.[10] Huang et al. also reported the formation of PbI_2 under a small electric field at the elevated temperature.[11] When exposed to the light and dry air, the halide anions generate free radicals, which deprotonate the methylammonium cation to form the highly volatile CH_3NH_2 molecules and PbI_2.[12] Xu et al. also observed the formation of hydrocarbons and NH_3 with the residuals of PbX_2 by light illumination-induced degradation for mixed-halide perovskites.[13]

S. L. Chen, Prof. J. Cao, Prof. J. C. Feng, Prof. J. L. Qi
State Key Laboratory of Advanced Welding and Joining
Harbin Institute of Technology
Harbin 150001, China
E-mail: jlqi@hit.edu.cn

S. L. Chen, Z. Hua, Dr. J. M. Zhang, Prof. P. Gao
Electron Microscopy Laboratory
School of Physics
Peking University
Beijing 100871, China
E-mail: p-gao@pku.edu.cn

Y. Zhang, Prof. J. J. Zhao, Z. W. Zhao, X. Su
School of Materials Science and Engineering
School of Mechanical Engineering
Shijiazhuang Tiedao University
Shijiazhuang 050043, China
E-mail: jinjinzhao2012@163.com

X. W. Zhang, Prof. P. Gao
International Center for Quantum Materials
School of Physics
Peking University
Beijing 100871, China

Prof. X. Wang, Prof. J. Y. Li
Shenzhen Key Laboratory of Nanobiomechanics
Shenzhen Institutes of Advanced Technology
Chinese Academy of Sciences
Shenzhen 518055, China
E-mail: jy.li1@siat.ac.cn

Prof. X. Z. Li, Prof. P. Gao
Collaborative Innovation Center of Quantum Matter
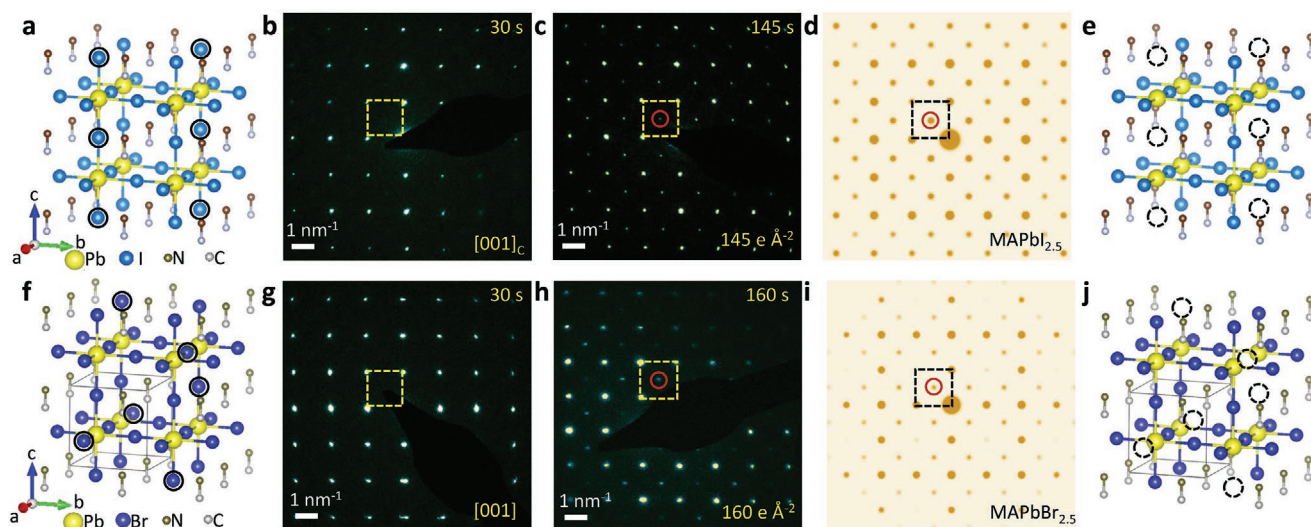E-mail: Beijing 100871, China

2001107 (1 of 7)

Figure 1. Forming superstructures in MAPbI$_3$ and MAPbBr$_3$. a) Atomistic structure of tetragonal MAPbI$_3$ viewing along its [110] direction to better compare with that of cubic MAPbBr$_3$. b) Electron diffraction (ED) pattern along the [001]$_C$ direction. c) The observed ED of superstructure phase with additional reflections highlighted by the red circle. d) The simulated ED of superstructure phase MAPbI$_{2.5}$ and e) the corresponding atomistic structure with ordered iodine vacancies, as indicated by the dashed circles. f) Atomistic structure of MAPbBr$_3$ and g) its ED pattern along the [001] direction. h) The observed ED pattern with additional reflections, highlighted by the red circle. i) The simulated ED of superstructure phase MAPbBr$_{2.5}$ and j) the corresponding atomistic structure with ordered bromine vacancies, marked by the dashed circles.

Although many such efforts have been made to reveal the final decomposition of products of MAPbI$_3$, the general decomposition pathway (i.e., how structure evolves during the degradation process) for OIHPs still remains largely elusive due to the difficulty in obtaining direct structural evidences during decomposition.

Transmission electron microscopy (TEM) based techniques are powerful tools to explore the mechanistic understanding of the materials, functionalities as well as their degradation mechanisms.[14,15] In some cases, the electron beam can transfer energy to the materials under illumination,[16–19] driving ions diffusion and structure evolution similar to heat- or light-induced phase transformation in the practical devices, giving us useful insights into how the device fails, and how we can improve it.[20,21] For example, it was found that under electron irradiation MAPbI$_3$ decomposes into PbI$_2$ with the escape of gaseous like NH$_3$ and HI,[17] which is consistent with the degradation process observed under heating[7,8] and light illumination[13] as well as the first principle calculations.[22] Alberti et al. unveiled that electron beam could cause polycrystalline MAPbI$_3$ decompose into PbI$_2$ nano-fragmentations and Pb clustering inside the MAPbI$_3$ boundary.[23] The formation of Pb has also been observed under high temperature annealing.[7] While many of these works concerned the final products of decomposed OIHPs, in our previous study, we observed an intermediate superstructure of MAPbI$_3$ along its decomposition pathway to PbI$_2$.[24] The generality of such superstructure and degradation pathway for OIHPs, however, is unclear and how to improve the stability of OIHPs remains to be explored.

In this work, we use in situ selected-area electron diffraction (SAED) with controlled low dose of electron illumination and scanning electron microscopy (SEM) techniques along with the energy-dispersive X-ray (EDS) analysis to study the general electron-beam-induced structure evolution of the OIHPs, based

on which we further propose strategies to suppress the decomposition of OIHPs. First, we uncover that the superstructure is more general instead of an exception in OIHPs, observed not only in tetragonal MAPbI$_3$ but also in cubic MAPbBr$_3$ and inorganic CsPbBr$_3$. We then identify a general decomposition pathway from MAPbX$_3$ to PbX$_2$ with anion-vacancy ordered MAPbX$_{2.5}$ superstructures in between. Finally, we demonstrate that the carbon coating on OIHPs can substantially slow down the decomposition into PbI$_2$ by stabilization of the perovskite structure framework. Our study reveals a general decomposition pathway of OIHPs that can be suppressed by carbon coating, likely offering insights into improving stability of perovskite solar cells (PSCs).

The atomistic structure of tetragonal MAPbI$_3$ is schematically shown in **Figure 1**a, and the corresponding SAED pattern presented in Figure 1b matches the ideal MAPbI$_3$ structure well, acquired from the pristine MAPbI$_3$ crystal (Figure S1, Supporting Information) grown on glass/FTO/TiO$_2$ substrate.[25] Additional superstructure reflections emerge with increased beam illumination dose, one of which is indicated by the red circle in Figure 1c that, however, is forbidden in tetragonal MAPbI$_3$, as we reported earlier.[24] While both the octahedral tilt[26,27] and ordered vacancies[28] can lead to superstructure diffraction spots in perovskite oxides, for MAPbI$_3$ we interpret such superstructure as vacancies ordering, since OIHPs are prone to lose negatively charged halide ions under electron beam illumination.[29] Indeed, the simulated ED patterns (Figure 1d) of the MAPbI$_{2.5}$ with ordered iodine vacancies (Figure 1e) exactly match the experimental ED patterns along both [001]$_C$ (Figure 1c) and [110]$_C$ (Figure S2, Supporting Information) directions (subscript C denotes pseudocubic index), and such superstructure has in fact been reported in a variety of perovskite oxides in the form of ABO$_{2.5}$.[28] The observation thus raises an important question that if the superstructure is general in OIHPs as well.

To answer this question, we also examine the structure of $MAPbBr_3$, another important OIHPs material that is cubic instead of tetragonal.[30,31] The atomistic structure of cubic $MAPbBr_3$ is schematically shown in Figure 1f, with the corresponding SAED pattern in Figure 1g acquired from the pristine $MAPbBr_3$ crystal (Figure S3, Supporting Information). Similar to $MAPbI_3$, additional superstructure diffraction reflections also appear under increased dose of electron illumination as seen in Figure 1h, and likewise, the corresponding structure is interpreted as $MAPbBr_{2.5}$ with ordered bromine vacancies (Figure 1j), for which the simulated ED patterns (Figure 1i) match the experimental ones along both the [001] (Figure 1h) and [121] (Figure S4, Supporting Information) directions. Moreover, our preliminary study (Figure S5, Supporting Information) shows this intermediated superstructure is also observed for inorganic perovskite ($CsPbBr_3$), suggesting the ordered

vacancies in form of $ABO_{2.5}$ are more general in OIHPs and its all inorganic counterpart instead of just an exception in $MAPbI_3$, similar to those observed in perovskite oxides in the form of $ABO_{2.5}$.[28]

The ordered vacancies as revealed by the superstructure diffraction spots are resulted from the loss of halide elements under electron illumination, and thus are closely related to the decomposition of OIHPs. Indeed, under continuous beam illumination, we observe clear structural evolution of $MAPbI_3$ as exhibited by SAED patterns along the $[001]_C$ zone axis.[24] It starts with the pristine ideal structure at 30 e Å^{-2} (**Figure 2**a), and evolves to the superstructure with ordered vacancies at 163 e Å^{-2} as indicated by the purple triangle (Figure 2b). With further increased doses, the methylamine and iodine ions are continuously lost, leading to the crumble of the perovskite framework (Figure 2c), as indicated by the disappearance
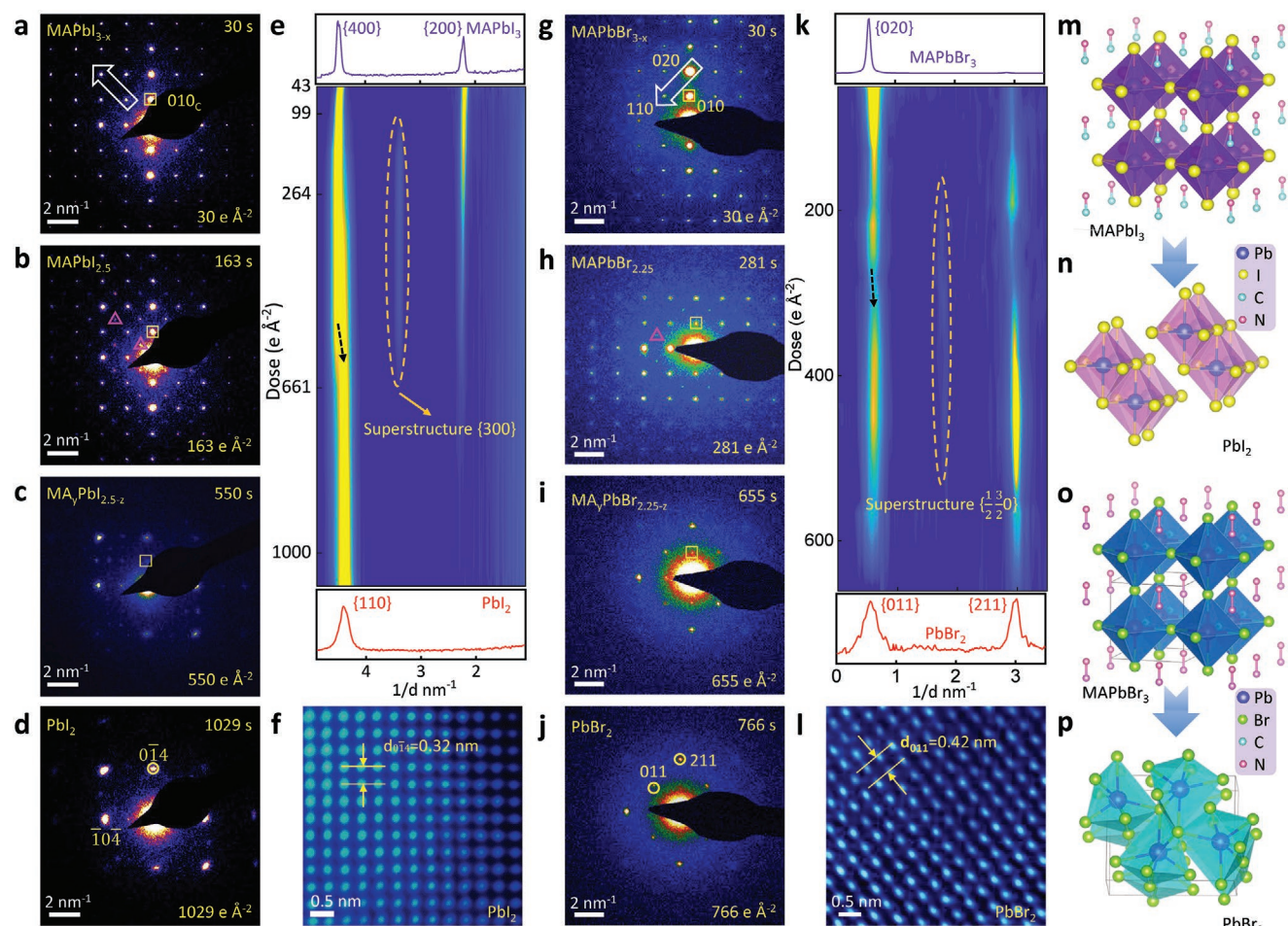

Figure 2. Generality of decomposition pathway for $MAPbI_3$ and $MAPbBr_3$. a–d) Consecutive SAED patterns during the decomposition from: a) $MAPbI_{3-x}$ $[001]_C$ zone axis ($0 < x < 0.5$), to: b) intermediate phase $MAPbI_{2.5}$, c) $MA_yPbI_{2.5-z}$ ($0 \le y \le 1$ and $0 \le z \le 0.5$), and d) PbI_2 [$\bar{4}41$] zone axis at a dose rate of 1 e Å^{-2} s^{-1}. The purple triangles in (b) highlight the superstructure reflections. e) The intensity line profiles extracted along the white arrow in (a). The top and bottom planes show the line profiles of $MAPbI_3$ and PbI_2, respectively. The yellow dashed ellipse highlights the lifespan of superstructure. f) The HAADF-STEM image of the decomposed product PbI_2 along the [$\bar{4}41$] zone axis. g–j) Time-series SAED patterns during the decomposition from: g) $MAPbBr_{3-x}$ [001] zone axis ($0 < x < 0.5$), to h) intermediate phase $MAPbBr_{2.5}$ with superstructure reflections highlighted by the purple triangle, i) $MA_yPbBr_{2.25-z}$ ($0 \le y \le 1$ and $0 \le z \le 0.5$), and j) $PbBr_2$ [01$\bar{1}$] zone axis at a dose rate of 1 e Å^{-2} s^{-1}. k) The intensity line profiles obtained from time-series SAED patterns along the white arrow in (g). The top and bottom planes show the line profiles of $MAPbBr_3$ and $PbBr_2$. The yellow dashed ellipse indicates the lifespan of superstructure. l) HRTEM image of the decomposed product $PbBr_2$. m–p) The structure illustrations for decomposition from $MAPbI_3$ to PbI_2 and $MAPbBr_3$ to $PbBr_2$. The structure of tetragonal $MAPbI_3$ is viewed along its [110] direction to better compare with that of cubic $MAPbBr_3$.

2001107 (3 of 7)

**ADVANCED
SCIENCE NEWS**

www.advancedsciencenews.com

**ADVANCED
MATERIALS**

www.advmat.de

of $(010)_C$ spot highlighted by the yellow square, and eventual decomposition into PbI_2 (Figure 2d). The line profiles extracted from the time-series SAED patterns are plotted as a function of irradiation dose in Figure 2e, revealing the decomposition pathway under electron beam illumination. In particular, the superstructure reflection $\{300\}$ emerges at ≈ 99 e Å^{-2}, and disappears at ≈ 661 e Å^{-2}. In the end the material is completely decomposed into PbI_2, as revealed by the appearance of PbI_2 $\{110\}$ peak, as well as the high angle annular dark field scanning TEM (HAADF STEM) image of decomposed PbI_2 in Figure 2f along the $[\bar{4}41]$ direction. It is worthy to note that the $\{220\}$ reflections of the tetragonal $MAPbI_3$ are very easy to be mistaken as the $\{014\}$ diffraction spots of hexagonal PbI_2 [32–37] (space group: R-3m:H, $a = b = 0.4557$ nm, $c = 2.0937$ nm, $\alpha = \beta = 90°$, and $\gamma = 120°$) due to their very close plane distances (Figure S6, Supporting Information).

To understand the generality of the observed decomposition pathway, we also investigate the structural evolution of cubic $MAPbBr_3$ as revealed by its consecutive SAED patterns in Figure 2g–j. During the decomposition, we again first observe an intermediate phase with superstructure spots marked by the purple triangle in Figure 2h, after which the structure keeps losing methylamine and bromine, resulting in collapse of perovskite structure (Figure 2i), and eventual decomposition into $PbBr_2$ along $[01\bar{1}]$ zone axis (Figure 2j). This is very similar to the process observed in $MAPbI_3$, which is also made evident by the evolution of intensity line profiles extracted from time-series SAED patterns (Figure 2k). Here the lifespan of the superstructure diffraction spot $(\frac{1}{2}\frac{3}{2}0)$ is highlighted by the yellow dashed ellipse from 160 to 531 s (≈ 160–531 e Å^{-2}), while the (020) peak of $MAPbBr_3$ gradually evolves into (011) peak of $PbBr_2$. The decomposed $PbBr_2$ is further confirmed by the high resolution TEM (HRTEM) image in Figure 2l and the quantitative EDS mapping in Figure S7, Supporting Information. Therefore, the results above show that the decomposition of the OIHPs, regardless of being cubic or tetragonal, starts with the loss of ordered halogen ions, followed by the loss of remaining halogen and methylamine ions, leading to eventual crumble of perovskite framework and decomposition into PbX_2 (Figure 2m–p). These degradation processes are likely predominantly caused by the radiolysis damage due to the semi-conduct nature of $MAPbX_3$.[38] During the radiolysis, the incoming electrons can transfer several eV to hundreds of eV to the atomic electrons, leaving many holes in valence band or inner shell, and resulting in the breakage of the chemical bonds, the loss of the crystallinity and the escape of the light atoms.[39] The transferred energy can further transfer to the atomic nuclei through phonons,[40] leading to the atomic displacement, as observed for halogen in alkali halides.[41] Secondary effects (mainly secondary electrons) account for a major part of this damage, since the emission of secondary electrons and electrostatic charge can lead to the drift of ions, mass transport or even complete destruction of the specimen due to the electrostatic forces.[42] This general decomposition pathway is important for understanding and improving the stability of PSCs despite that the degradation in the practical devices might be more complicated as it not only happens inside the OIHPs but also at the interfaces.

In fact, it is vitally important to stabilize the structure of OIHPs for enhanced stability of PSCs, and previous reports have shown that coating could be effective to certain extent,[43–45] though its microscopic mechanism is not clear. In order to understand this effect, we coat a thin carbon layer about 6–10 nm thick on $MAPbI_3$, as shown in **Figure 3**a, while there is almost no amorphous contrast for the specimen without carbon coat (Figure S8, Supporting Information). The time-series of SAED patterns in Figure 3d–g present the degradation pathway along the $[110]_C$ direction of uncoated $MAPbI_3$, starting with initial $MAPbI_3$, through the same intermediated superstructure $MAPbI_{2.5}$ to the final PbI_2 (Figure 3b; Figure S9, Supporting Information). During the degradation, remarkably, the characteristic $(002)_C$ reflection of perovskite in the carbon coated $MAPbI_3$ (C@$MAPbI_3$) in Figure 3h–k maintains at 7600 e Å^{-2}, while in sharp contrast it only survives at 791 e Å^{-2} (Figure 2g) in $MAPbI_3$ without coating, suggesting the suppression of degradation of the perovskite structure framework by carbon coating. This can be better appreciated from comparison of characteristic $(002)_C$ diffraction intensity versus time between coated and uncoated $MAPbI_3$ shown in Figure 3c. The intensity of $MAPbI_3$ $(002)_C$ increases initially due to an on-axis adjust, then gradually decreases and finally disappears while $(002)_C$ diffraction intensity of C@$MAPbI_3$ gradually increases and keeps at a stable value, suggesting the perovskite framework is maintained. The time-series of SAED patterns along the $[001]_C$ direction (Figure S10, Supporting Information; Figure 2a–d) also confirm the conclusion that carbon coating can stabilize the $MAPbI_3$ structure framework and thus suppress the degradation of $MAPbI_3$. This likely explains the better stability of OIHPs with coating and thus improved stability of PSCs. Since the thin carbon coating layer makes negligible effects on electron scattering (see Supporting Information for a detailed discussion), it is believed the coating enhanced stability is because the coating layer can serve as a diffusion barrier, reducing the escape rate of the volatile species (e.g., halogen atom and CH_3NH_2),[29,41] as proved by both experimental results and DFT calculations [33] and the EDS results (shown later). Moreover, for one-side coated specimen with half of shielding, the degradation is not slowed down (Figure S11, Supporting Information), likely because the volatile species can escape from the other uncoated side.

The suppression of degradation by carbon coating is also revealed by the evolution of morphology and composition of C@$MAPbI_3$ in comparison to $MAPbI_3$ without carbon coating, as shown in **Figure 4**. The dimensions of C@$MAPbI_3$ are quite stable, showing less than 2% change (Figure 4i), while substantial shrinkage is observed for $MAPbI_3$ without coating approximately 10% along the longitudinal direction and 5% along the transverse direction. Correspondingly, the I/Pb atomic ratio decreases from pristine 2.93 and is stabilized at 2.40 for C@$MAPbI_3$ (Figure 4j), consistent with the suppression of the degradation, while that of $MAPbI_3$ quickly drops to 1.96, consistent with decomposed product PbI_2. This again demonstrates the effectiveness of carbon coating in slowing down decomposition of $MAPbI_3$, which can be understood from the suppression of the degradation as presented in Figure 3.

Our work reveals a general decomposition pathway for both tetragonal $MAPbI_3$ and cubic $MAPbBr_3$ under the electron beam illumination through an intermediate superstructure $MAPbX_{2.5}$ to the final PbX_2. It turns out that such superstructure is quite common in perovskite oxides, yet not recognized until our
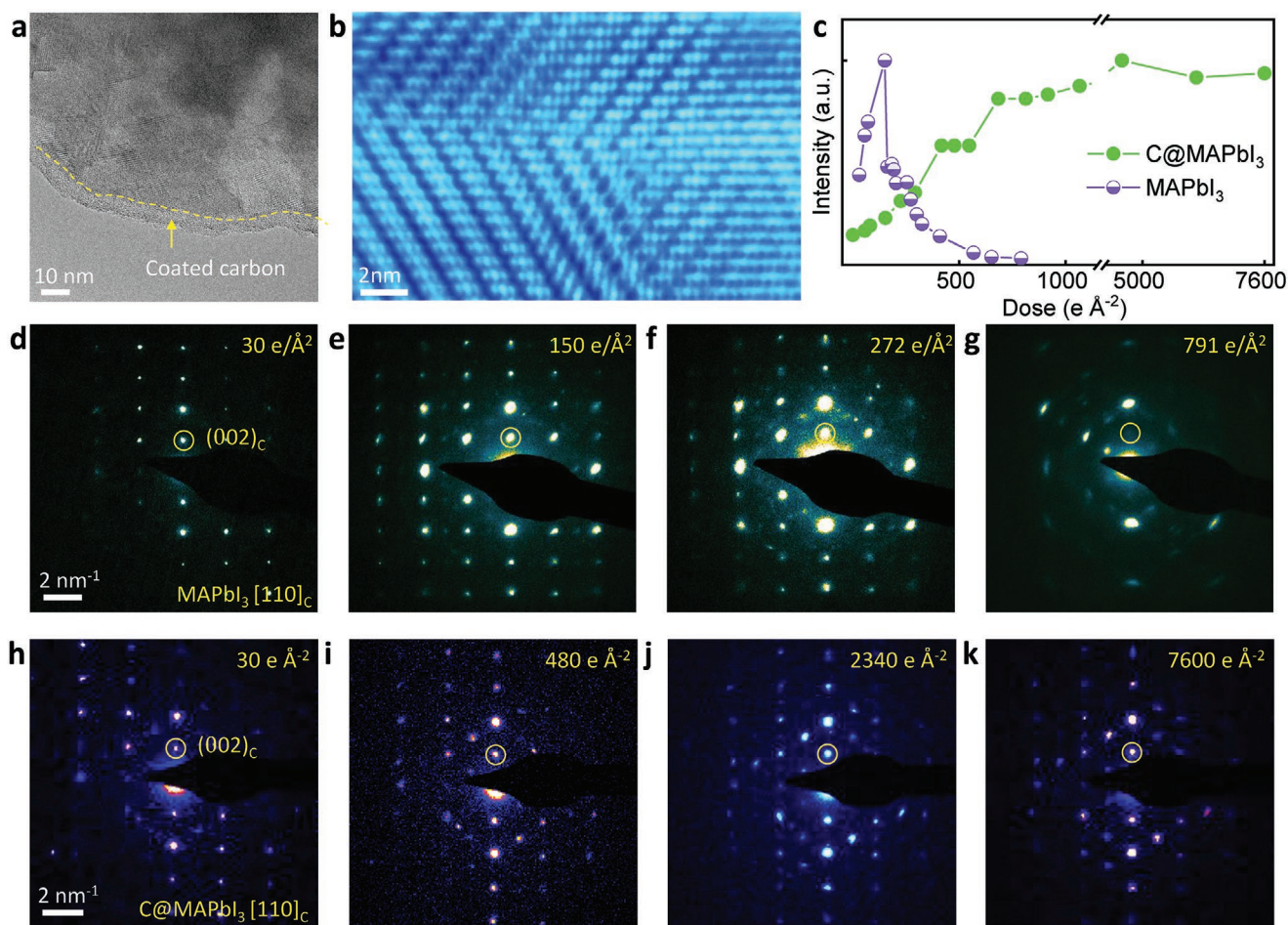
**ADVANCED
SCIENCE NEWS**

www.advancedsciencenews.com

**ADVANCED
MATERIALS**

www.advmat.de

Figure 3. Suppression of degradation. a) HRTEM image with a 6–10 nm carbon layer coated on MAPbI$_3$. b) HAADF STEM image of PbI$_2$ along the [110] direction. c) The intensities of (002)$_C$ reflection are plotted as a function of time. d–g) Time-series SAED patterns at 30, 150, 272, 791 s along the [110]$_C$ direction of MAPbI$_3$ with the total dose. h–k) Consecutive SAED patterns at 30, 480, 2340, 7600 s along the [110]$_C$ direction of C@MAPbI$_3$ with total dose. The dose rate is 1 e Å^{-2} s^{-1} at 300 kV for SAED imaging. (002)$_C$ spots are marked by the yellow circles in (d)–(g) for MAPbI$_3$ and (h)–(k) for C@MAPbI$_3$ along the [110]$_C$ direction.

studies. We further show that carbon coating can effectively stabilize the perovskite framework and suppress the decomposition. The coating is likely to impede the continuous loss of ions and thus prevent the collapse of the structural framework of perovskite, resulting in suppression of the degradation. We believe such insights will be useful to design more stable PSCs.

Furthermore, in situ TEM techniques have been used to visualize the working process and reveal the degradation mechanism of OIHPs under external stimuli,[14] and it is important to quantify the effect of the electron beam irradiation itself on the structural instability. In this regard, our study not only reveals the mechanistic structure evolution of OIHPs under electron beam irradiation, but also quantifies the critical dose for structural transformation, which can help guide future study via in situ electron microscopy.

Experimental Section

MAPbI$_3$ Synthesis: PbI$_2$ and CH$_3$NH$_3$I (molar ratio 1:1) were dissolved in γ-butyrolactone (GBL) with the concentration of 1.3 mol L^{-1}, prior to stirring in 12 h at the 70 °C. The CH$_3$NH$_3$PbI$_3$ precursor solution was

obtained and filtered using polytetrafluoroethylene (PTFE) filter with 0.22 μm pore size. The Fluorine-doped tin oxide (FTO)/TiO$_2$ substrates were face to face clamped together at fixed distance of 50–200 μm. The fixed FTO/TiO$_2$ substrates were vertically and partially soaked in a 10 mL MAPbI$_3$ precursor solution at 120 °C, and then the feeding MAPbI$_3$ precursor solution was added twice a day in the nitrogen glove box. After 17 days, the substrates with MAPbI$_3$ single crystal film were taken out, and then dried at 120 °C for 10 min in nitrogen.

MAPbBr$_3$ Synthesis: PbBr$_2$ and CH$_3$NH$_3$Br were dissolved in N,N-dimethylformamide (DMF) and stirred at 30 °C for 12 h to obtain 1 mol L^{-1} MAPbBr$_3$ precursor solution. The MAPbBr$_3$ precursor solution was purified by polytetrafluoroethylene (PTFE) filter with 0.22 μm pore size, and then heated to 95 °C in a 10 mL container in dark environment. The container could be taken out by daylight at 30–50% humidity until the MAPbBr$_3$ single crystals were grown after one night.[46]

TEM Samples Preparation: All TEM samples were prepared in an argon-filled glovebox to avoid side reactions. First, samples from substrate were scratched and dispersed into anhydrous ether. Then, the clear suspensions were deposited on holey carbon copper girds. The carbon copper girds were sealed with a plastic bag full of argon before transforming into the TEM column. The carbon layer was coated on one or both sides of as-prepared samples using Ar ion to sputter carbon target at 8 k eV and 200 pA by a precision etching coating system (Gatan Model 682).
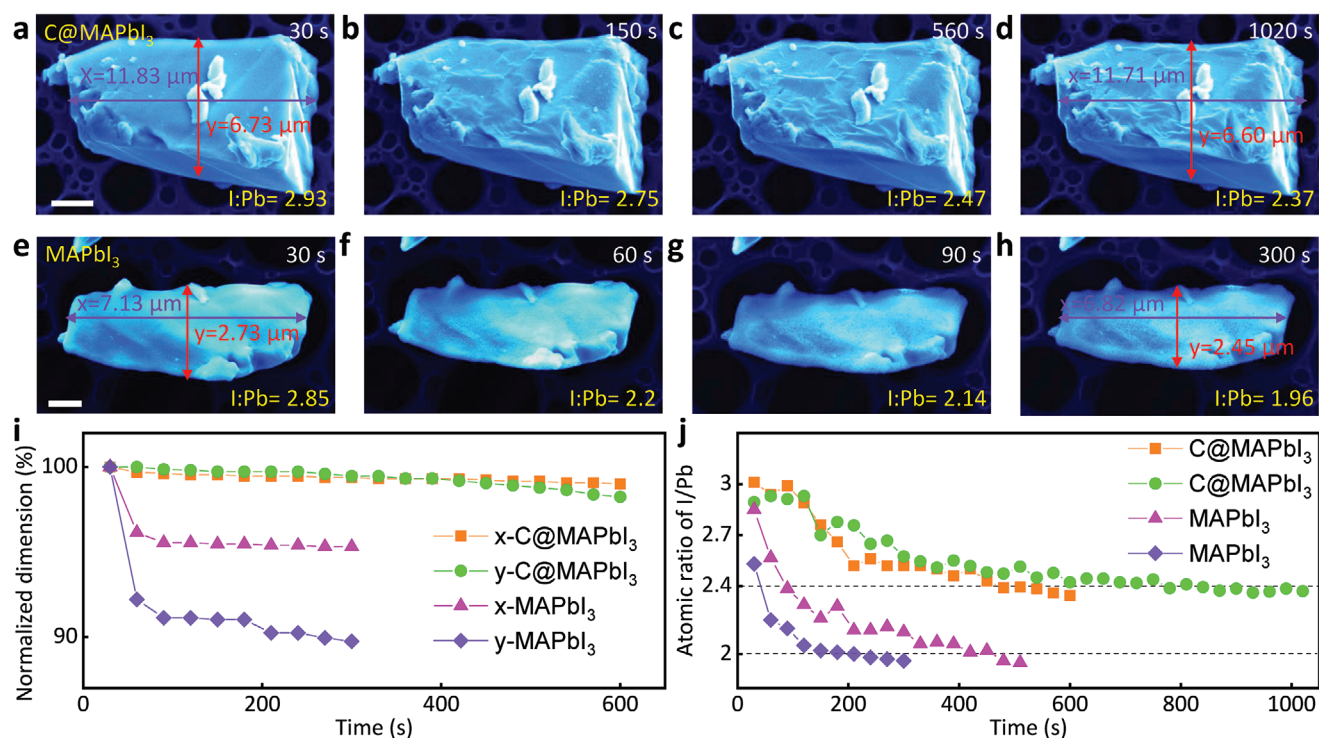
**ADVANCED
SCIENCE NEWS**

www.advancedsciencenews.com

**ADVANCED
MATERIALS**

www.advmat.de

Figure 4. Morphology and composition evolutions. a–h) Consecutive SEM images showing the morphology and composition evolutions of C@MAPbI$_3$ (a–d) and MAPbI$_3$ (e–h) during continuous electron beam illumination at 10 kV. The dose rate is about 6–12 e Å^{-2} s^{-1}. Thus the estimated doses are about 270, 1350, 5040, and 9180 e Å^{-2} for (a)–(d) and 270, 540, 810, and 2700 e Å^{-2} for (e)–(h) based on an average dose rate 9 e Å^{-2} s^{-1}. i) The normalized dimensions of C@MAPbI$_3$ and MAPbI$_3$ are plotted as a function time. The distance of "x" and "y" are marked in (a) and (e). j) I/Pb atomic ratio obtained from the quantitative SEM-EDS analysis is plotted as a function of time.

Characterization: Powder XRD patterns were obtained on D8 Advance diffractometer using Cu Kα radiation (40 kV and 40 mA) with a scanning rate of 4° min^{-1} for wide-angle test increment. The SAED patterns, HRTEM, STEM images and the corresponding EDS mappings were conducted at an aberration corrected FEI (Titan Cubed Themis G2) operated at 300 kV equipped with an XFEG gun and Bruker Super-X EDS detectors. The current was typically about 20–30 pA for STEM, 2–3 nA for HRTEM. As for all SAED images, the typical current was about 1–1.2 nA and the experimental operations take about 30 s to record the first SAED patterns including moving the sample into sight and setting the aperture. The simulated ED patterns were obtained by the SingleCrystal (Crystalmaker).

The morphology and composition of the sample were performed by SEM (FEI Quanta 200F). The SEM-EDS was carried out at 10 kV and each spectrum was acquired from a ≈50 μm^2 for Figure 4a–d and 20 μm^2 for Figure 4e–h area at ≈8000–10000 count per second for about 30 s using a current of ≈8–10 nA, corresponding to a dose rate of 6–12 e Å^{-2} s^{-1}. It took 30 s to acquire each spectrum for quantitative analysis, which is treated as an average I/Pb atomic ratio for each 30 s. Thus tens of such atomic I/Pb ratio can present the chemical evolution during the whole decomposed process. The quantitative EDS analysis was performed on AZtec software from Oxford Instruments Nanotechnology Limited, which uses the same factory standards of each element to determine the content, as shown in Figure S12, Supporting Information. To further check the accuracy of the quantitative analysis, SEM-EDS was carried out for the PbI$_2$ reagent (99.9% from Macklin) with the similar acquiring condition to that for MAPbI$_3$ and C@MAPbI$_3$. The atomic ratio of I/Pb ranges from 2.01 to 2.10 (Figure S13, Supporting Information), which basically matches the expected value 2.00.

The surface, exposure time, and dose information are included in the captions for each Figure. The irradiation should be very uniform for both of SAED and TEM with parallel illumination, which can be ensured by the three-condenser-system of Titan Cubed Themis G2. Under STEM and SEM experiments, the focused electron beam fast scans the whole irradiation region with an even electron dose, thus also presenting a uniform irradiation.

Supporting Information

Supporting Information is available from the Wiley Online Library or from the author.

Acknowledgements

Conflict of Interest

The authors declare no conflict of interest.

Author Contributions

S.L.C. and Y.Z. contributed equally to this work. P.G., J.L., J.Q., and J.Z. conceived and supervised the project. S.C. carried out TEM-related experiments and analyzed TEM data with the direction of P.G.; Y.Z., Z.Z., and X.S. synthesized the crystals. S.C. and Y.Z. performed the SEM and XRD measurements; X.Z. and X.W. constructed the structure of superstructure phase with the help of X.L.; Z.H. conducted carbon coating. J.C., J.F., and J.Q. provided crystals. S.C., J.L., and P.G. wrote the manuscript and all authors participated in the discussions.

Keywords

[1] A. Kojima, K. Teshima, Y. Shirai, T. Miyasaka, *J. Am. Chem. Soc.* **2009**, *131*, 6050.

[2] National Renewable Energy Laboratory (NREL), Efficiency records chart, https://www.nrel.gov/pv/cell-efficiency.html (accessed: April 2020).

[3] N. Li, S. Tao, Y. Chen, X. Niu, C. K. Onwudinanti, C. Hu, Z. Qiu, Z. Xu, G. Zheng, L. Wang, *Nat. Energy* **2019**, *4*, 408.

[4] X. Wu, L. Z. Tan, X. Shen, T. Hu, K. Miyata, M. T. Trinh, R. Li, R. Coffee, S. Liu, D. A. Egger, I. Makasyuk, Q. Zheng, A. Fry, J. S. Robinson, M. D. Smith, B. Guzelturk, H. I. Karunadasa, X. Wang, X. Zhu, L. Kronik, A. M. Rappe, A. M. Lindenberg, *Sci. Adv.* **2017**, *3*, e1602388.

[5] D. Bryant, N. Aristidou, S. Pont, I. Sanchez-Molina, T. Chotchunangatchaval, S. Wheeler, J. R. Durrant, S. A. Haque, *Energy Environ. Sci.* **2016**, *9*, 1655.

[6] T. A. Berhe, W. Su, C. Chen, C. Pan, J. Cheng, H. Chen, M. Tsai, L. Chen, A. A. Dubale, B. Hwang, *Energy Environ. Sci.* **2016**, *9*, 323.

[7] W. Huang, S. Sadhu, S. Ptasinska, *Chem. Mater.* **2017**, *29*, 8478.

[8] S. Kim, S. Bae, S. Lee, K. Cho, K. D. Lee, H. Kim, S. Park, G. Kwon, S. Ahn, H. Lee, *Sci. Rep.* **2017**, *7*, 1200.

[9] N. Kim, Y. H. Min, S. Noh, E. Cho, G. Jeong, M. Joo, S. Ahn, J. S. Lee, S. Kim, K. Ihm, *Sci. Rep.* **2017**, *7*, 4645.

[10] Q. Jeangros, M. Duchamp, J. Werner, M. Kruth, R. E. Dunin-Borkowski, B. Niesen, C. Ballif, A. Hessler-Wyser, *Nano Lett.* **2016**, *16*, 7013.

[11] Y. Yuan, Q. Wang, Y. Shao, H. Lu, T. Li, A. Gruverman, J. Huang, *Adv. Energy Mater.* **2016**, *6*, 1501803.

[12] G. Abdelmageed, L. Jewell, K. Hellier, L. Seymour, B. Luo, F. Bridges, J. Z. Zhang, S. Carter, *Appl. Phys. Lett.* **2016**, *109*, 233905.

[13] R. Xu, Y. Li, T. Jin, Y. Liu, Q. Bao, C. O Carroll, J. Tang, *ACS Appl. Mater. Interfaces* **2018**, *10*, 6737.

[14] F. U. Kosasih, C. Ducati, *Nano Energy* **2018**, *47*, 243.

[15] Y. Zhou, H. Sternlicht, N. P. Padture, *Joule* **2019**, *3*, 641.

[16] C. Xiao, Z. Li, H. Guthrey, J. Moseley, Y. Yang, S. Wozny, H. Moutinho, B. To, J. J. Berry, B. Gorman, Y. Yan, K. Zhu, M. Al-Jassim, *J. Phys. Chem. C* **2015**, *119*, 26904.

[17] A. R. Milosavljević, W. Huang, S. Sadhu, S. Ptasinska, *Angew. Chem., Int. Ed.* **2016**, *55*, 10083.

[18] N. Klein-Kedem, D. Cahen, G. Hodes, *Acc. Chem. Res.* **2016**, *49*, 347.

[19] H. Yuan, E. Debroye, K. Janssen, H. Naiki, C. Steuwe, G. Lu, M. Moris, E. Orgiu, H. Uji-i, F. De Schryver, P. Samorì, J. Hofkens, M. Roeffaers, *J. Phys. Chem. Lett.* **2016**, *7*, 561.

[20] G. Huang, C. Huang, N. Kumar, C. Huang, T. Tseng, W. Wu, *J. Mater. Chem. A* **2020**, *8*, 648.

[21] B. Wei, X. Lu, F. Voisard, H. Wei, H. Chiu, Y. Ji, X. Han, M. L. Trudeau, K. Zaghib, G. P. Demopoulos, R. Gauvin, *ACS Appl. Energy Mater.* **2018**, *1*, 3180.

[22] Y. Xue, Y. Shan, H. Xu, *J. Chem. Phys.* **2017**, *147*, 124702.

[23] A. Alberti, C. Bongiorno, E. Smecca, I. Deretzis, A. La Magna, C. Spinella, *Nat. Commun.* **2019**, *10*, 2196.

[24] S. Chen, X. Zhang, J. Zhao, Y. Zhang, G. Kong, Q. Li, N. Li, Y. Yu, N. Xu, J. Zhang, K. Liu, Q. Zhao, J. Cao, J. Feng, X. Li, J. Qi, D. Yu, J. Li, P. Gao, *Nat. Commun.* **2018**, *9*, 4807.

[25] J. Zhao, G. Kong, S. Chen, Q. Li, B. Huang, Z. Liu, X. San, Y. Wang, C. Wang, Y. Zhen, H. Wen, P. Gao, J. Li, *Sci. Bull.* **2017**, *62*, 1173.

[26] M. U. Rothmann, W. Li, Y. Zhu, A. Liu, Z. Ku, U. Bach, J. Etheridge, Y. Cheng, *Adv. Mater.* **2018**, *30*, 1800629.

[27] D. I. Woodward, I. M. Reaney, *Acta Crystallogr., Sect. B: Struct. Sci.* **2005**, *61*, 387.

[28] J. H. Jang, Y. Kim, Q. He, R. Mishra, L. Qiao, M. D. Biegalski, A. R. Lupini, S. T. Pantelides, S. J. Pennycook, S. V. Kalinin, A. Y. Borisevich, *ACS Nano* **2017**, *11*, 6942.

[29] R. F. Egerton, P. Li, M. Malac, *Micron* **2004**, *35*, 399.

[30] W. Zhang, L. Peng, J. Liu, A. Tang, J. Hu, J. Yao, Y. S. Zhao, *Adv. Mater.* **2016**, *28*, 4040.

[31] H. Rao, W. Li, B. Chen, D. Kuang, C. Su, *Adv. Mater.* **2017**, *29*, 1602639.

[32] G. Divitini, S. Cacovich, F. Matteocci, L. Cinà, A. Di Carlo, C. Ducati, *Nat. Energy* **2016**, *1*, 15012.

[33] Z. Fan, H. Xiao, Y. Wang, Z. Zhao, Z. Lin, H. Cheng, S. Lee, G. Wang, Z. Feng, W. A. Goddard, Y. Huang, X. Duan, *Joule* **2017**, *1*, 548.

[34] H. Zhu, J. Fu, F. Meng, X. Wu, Z. Gong, Q. Ding, M. V. Gustafsson, M. T. Trinh, S. Jin, X. Zhu, *Nat. Mater.* **2015**, *14*, 636.

[35] M. Yang, Y. Zhou, Y. Zeng, C. Jiang, N. P. Padture, K. Zhu, *Adv. Mater.* **2015**, *27*, 6363.

[36] Y. Zhou, A. L. Vasiliev, W. Wu, M. Yang, S. Pang, K. Zhu, N. P. Padture, *J. Phys. Chem. Lett.* **2015**, *6*, 2292.

[37] F. Zhu, L. Men, Y. Guo, Q. Zhu, U. Bhattacharjee, P. M. Goodwin, J. W. Petrich, E. A. Smith, J. Vela, *ACS Nano* **2015**, *9*, 2948.

[38] R. F. Egerton, *Ultramicroscopy* **2013**, *127*, 100.

[39] R. F. Egerton, *Micron* **2019**, *119*, 72.

[40] L. W. Hobbs, *Quantitative Electron Microscopy*, Plenum Press, New York **1984**.

[41] R. F. Egerton, P. A. Crozier, P. Rice, *Ultramicroscopy* **1987**, *23*, 305.

[42] R. F. Egerton, *Microsc. Res. Tech.* **2012**, *75*, 1550.

[43] E. Bi, H. Chen, F. Xie, Y. Wu, W. Chen, Y. Su, A. Islam, M. Grätzel, X. Yang, L. Han, *Nat. Commun.* **2017**, *8*, 15330.

[44] E. L. Lim, C. C. Yap, M. H. H. Jumali, M. A. M. Teridi, C. H. Teh, *Nano-Micro Lett.* **2018**, *10*, 27.

[45] H. Kim, J. Lee, B. Kim, H. R. Byun, S. H. Kim, H. M. Oh, S. Baik, M. S. Jeong, *Sci Rep* **2019**, *9*, 15461.

[46] Y. Liu, Z. Yang, D. Cui, X. Ren, J. Sun, X. Liu, J. Zhang, Q. Wei, H. Fan, F. Yu, *Adv. Mater.* **2015**, *27*, 5176.